

PAPER • OPEN ACCESS

## A bending microactuator with large angular range for origami-inspired bidirectional folding

To cite this article: Lena Seigner *et al* 2025 *Smart Mater. Struct.* **34** 105031

View the [article online](#) for updates and enhancements.

### You may also like

- [Effective criteria for entanglement witnesses in small dimensions](#)  
ukasz Grzelka, ukasz Marcin Skowronek and Karol yczkowski
- [Advancing optical spiking neural networks with exciton-polaritons](#)  
Krzysztof Tyszk, Andrzej Opala and Barbara Pietka
- [Research on asynchronous quadrature integral demodulation method for amplitude modulation signal](#)  
Yan Ye and Pengcheng WANG



The Electrochemical Society  
Advancing solid state & electrochemical science & technology








**249th  
ECS Meeting**  
May 24-28, 2026  
Seattle, WA, US  
*Washington State  
Convention Center*

# Spotlight Your Science

***Submission deadline:  
December 5, 2025***

**SUBMIT YOUR ABSTRACT**

# A bending microactuator with large angular range for origami-inspired bidirectional folding

Lena Seigner<sup>1</sup> , Vincent Gottwald<sup>1</sup> , Lars Bumke<sup>2</sup> , Eckhard Quandt<sup>2</sup>   
and Manfred Kohl<sup>1,\*</sup> 

<sup>1</sup> Institute of Microstructure Technology, Karlsruhe Institute of Technology (KIT), Karlsruhe, Germany

<sup>2</sup> Department of Materials Science, Kiel University, Kiel, Germany

E-mail: [manfred.kohl@kit.edu](mailto:manfred.kohl@kit.edu)

Received 25 June 2025, revised 23 September 2025

Accepted for publication 28 September 2025

Published 23 October 2025



## Abstract

A bending microactuator with large angular range is presented consisting of a novel antagonistic design of cascaded shape memory alloy (SMA) hinges. The antagonistic design comprises two counteracting hinges with double-bridge design to enable bidirectional folding of a pair of rigid tiles serving as a building block of an origami-inspired microsystem. Additional connection of the hinges in series results in a cascaded design to enhance the bidirectional folding angle. A microfabrication process is developed using a combination of magnetron sputtering of TiNiCu films and UV photolithography. The strongly coupled thermo-mechanical properties of the SMA hinges are taken into account in finite element simulations to determine optimized hinge geometries, which allow for selective shape setting at either maximum or minimum bending angle to functionalize their performance as protagonists or antagonists. Thus, localized Joule heating enables folding and unfolding to discrete angles ensuring reversible and programmable folding motions. The bidirectional folding angles of the bending microactuators cover the range of about  $\pm 105^\circ$ , which is more than a factor of two compared to microactuators with single hinge design.

Supplementary material for this article is available [online](#)

Keywords: reprogrammable shape, shape memory alloy films, microtechnology, origami, microactuator, folding

## 1. Introduction

An innovative approach in the development of actuator systems is ‘programmable matter’ consisting of active components that can be programmed to dynamically change

their shape or function in order to carry out different tasks autonomously on demand. The engineering of programmable matter can be accomplished, for instance, by following the concept of origami, the ancient art of paper folding. An initial planar structure, composed of rigid, interconnected tiles, can be folded into various three-dimensional (3D) shapes through controlled bending movements at the joints. At the mini-ature scale, origami-inspired layouts allow the use of planar fabrication techniques, such as sputtering, photolithography, and laser cutting. Their ability to be compactly stored makes them suitable for applications with limited space, such as microrobotics [1, 2], advanced electronics [3, 4], metamaterial concepts [5] as well as implants and stents [6, 7]. The

\* Author to whom any correspondence should be addressed.



Original content from this work may be used under the terms of the [Creative Commons Attribution 4.0 licence](#). Any further distribution of this work must maintain attribution to the author(s) and the title of the work, journal citation and DOI.

2D structures can reach their final 3D shape on demand by self-folding [8–10]. The role of miniaturization is crucial in this context: The smaller the individual tiles, the finer and more complex the resulting 3D structures can be, providing enhanced functionality and precision.

Shape memory alloys (SMAs) are promising candidates for the realization of bending microactuators enabling origami-inspired folding in small dimensions with high bending moment and small radius of curvature [11–13]. Compared to other miniature-scale actuation methods such as liquid crystal elastomers [14] and shape memory polymers [15], SMAs offer a high work density, a favorable scaling behavior, and generate high stress [12]. SMA materials such as TiNi exhibit the one-way shape memory effect. In the low-temperature martensite phase, they can be quasi-plastically deformed. Afterwards, their previously imprinted memory shape can be recovered by heating the deformed material above a characteristic temperature regime, whereby they undergo a diffusionless and reversible phase transformation. Sputtered SMA films are already used in various high-bending applications such as self-expanding stents [16, 17], stretchable electronics [18, 19], and microvalves [20, 21].

The concept of origami-inspired programmable matter based on the folding of SMA hinges has been demonstrated at the macroscopic scale using tiles with edge lengths at centimeter dimensions [22, 23]. By introducing multistability, ambiguous folding branches are avoided and the final 3D shape is stabilized. However, programmable systems based on SMA materials are limited to unidirectional actuation [24]. Thus, after self-folding to an initial 3D shape the programmable sheet requires manual unfolding before another folding sequence can be performed to change the shape. An important extension of this concept is reprogrammable matter, which can reconfigure its 3D shape without manual intervention by self-unfolding. This performance requires a mechanism for resetting or counter-actuation in opposite direction. For instance, the actuator can be coupled with a biasing spring [25], or an antagonistic actuator may be utilized to realize bidirectional folding [26, 27]. Current reconfigurable SMA-based structures are restricted to macro-scale dimensions [28, 29]. At the micro scale, however, the concept of reprogrammable micromatter becomes a necessity as manual reconfiguration is hardly possible.

The development of bending microactuators for bidirectional folding involves a number of challenges. Mechanical coupling may limit the folding range considerably, as actuation of the protagonist SMA hinge causes unfolding and additional deformation of the antagonist SMA hinge. Furthermore, the close vicinity of the antagonistic SMA hinges may cause thermal cross-coupling, which leads to unwanted counter-actuation limiting the available work output. Previous work has proven the concept of combining two antagonistic TiNi hinges for bidirectional folding of tiles with millimeter dimensions [30–32]. Thereby, each TiNi hinge consists of a double-bridge structure that interconnects two tiles and can be selectively actuated by direct Joule heating. The memory shape of the TiNi hinges is adjusted by heat treatment in

constraint configuration at a bending angle of either  $+180^\circ$  for folding and  $-180^\circ$  for unfolding. Yet, for a hinge thickness of  $20\text{ }\mu\text{m}$ , only a total bidirectional folding range of about  $\pm 40^\circ$  is reached, which is attributed to limited maximum strain in the bending region, fabrication tolerances, as well as mechanical, and thermal coupling effects [31].

Here, we present a SMA film-based bending microactuator for bidirectional folding with a novel antagonistic design of cascaded SMA hinges, which meets the previous challenges of thermal cross-coupling and extends the bidirectional folding range beyond  $\pm 105^\circ$ . A model-based design is introduced taking into account the thermo-mechanical coupling of the SMA hinges. In addition, a dedicated fabrication process is presented and a novel procedure for local adjustment of the shape memory effect in each cascade is introduced.

## 2. Materials and methods

The SMA materials used for the fabrication of the bending microactuator are sputter-deposited Ti-rich TiNiCu films of  $6\text{ }\mu\text{m}$  thickness. TiNiCu thin films are of particular relevance for long-lifetime applications due to their small grain size, coherent precipitates, and good crystallographic compatibility over a wide compositional variation [33]. Sputter deposition of the films is performed onto a sacrificial Cu layer and a Ta adhesion layer on a Si wafer substrate. The films are released from the substrate by wet etching the sacrificial Cu layer. By rapid thermal annealing at  $700\text{ }^\circ\text{C}$  for 15 min in a vacuum chamber, the amorphous TiNiCu is crystallized and the martensitic phase transformation is adjusted. Further details on film fabrication are described in [34]. The heat treated TiNiCu films are characterized for their thermal, electrical, and mechanical properties. The deduced parameters are used in coupled electro-thermal finite element simulations, supporting the microactuator design.

### 2.1. Materials characterization

Figure 1 displays a DSC measurement of an as-received  $\text{Ti}_{53.9}\text{Ni}_{30.4}\text{Cu}_{15.7}$  film, which reveals the start/finish temperatures of martensitic phase transformation upon heating  $A_{sf}$  and cooling  $M_{sf}$ . At room temperature, the material is in martensitic state and transforms into austenite in the temperature range between  $A_s = 56\text{ }^\circ\text{C}$  and  $A_f = 69\text{ }^\circ\text{C}$ . Upon cooling, the reverse transformation takes place between  $M_s = 55\text{ }^\circ\text{C}$  and  $M_f = 45\text{ }^\circ\text{C}$ . For mechanical characterization of the TiNiCu films in a tensile test setup, dogbone samples are fabricated by photolithography and clamped in a custom sample holder. Figure 2 shows stress-strain curves of the uniaxially loaded samples at the strain rate of  $10^{-4}\text{ s}^{-1}$  for three different temperatures carried out in a heating chamber. The material behavior is characterized by an elastic loading path, followed by a plateau-like increase of stress at a specific yield stress. At  $23\text{ }^\circ\text{C}$ , the SMA film is in martensitic state. In this case, the

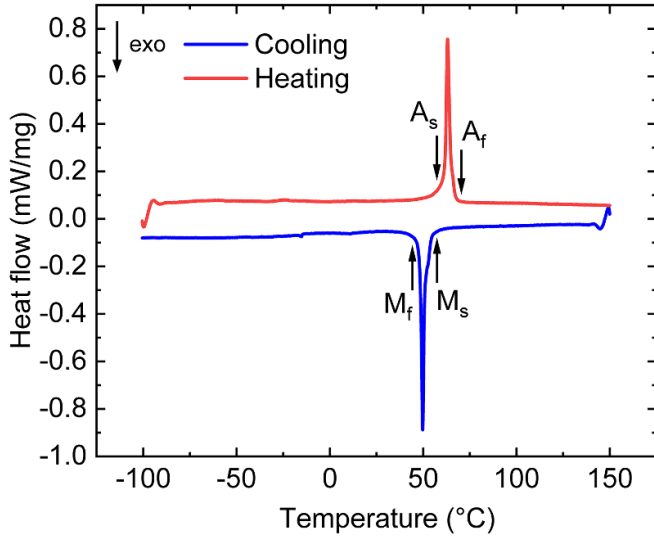


**Figure 1.** Differential scanning calorimetry measurement of 6  $\mu\text{m}$  thick TiNiCu film. The start/finish phase transformation temperatures of martensite ( $M_s/M_f$ ) and austenite phase ( $A_s/A_f$ ) are indicated.

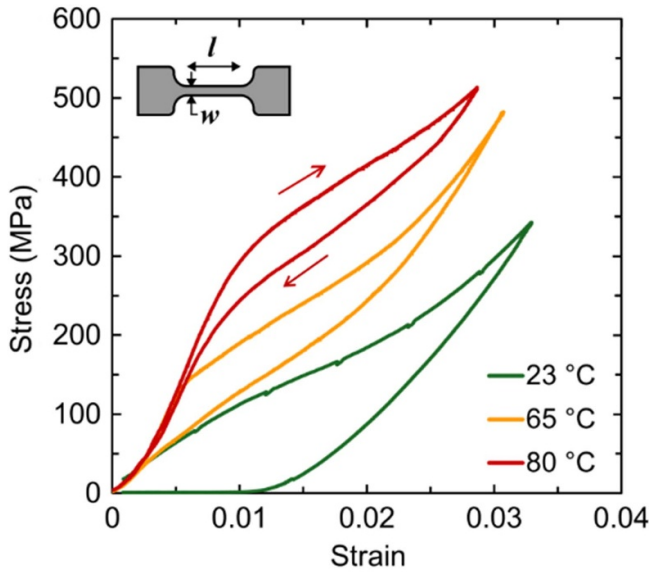


**Figure 2.** Tensile stress-strain characteristics of a dogbone-shaped TiNiCu test sample of 6  $\mu\text{m}$  thickness at different temperatures as indicated at a strain rate of  $10^{-4} \text{ s}^{-1}$ . The lateral dimensions of the sample are  $l = 6 \text{ mm}$  and  $w = 1 \text{ mm}$ .

stress-strain characteristic exhibits a typical nonlinear quasi-plastic behavior, caused by the accommodation of martensite variants upon loading. After reaching the investigated strain of 3% and subsequent load release, a remanent strain of approximately 1% occurs, which can be reset by heating the specimen above the austenite finish temperature  $A_f$ . At 65 and 80  $^{\circ}\text{C}$ , the sample shows a superelastic stress-strain behavior and recovers the full transformation strain upon unloading. At the strain rate of  $10^{-4} \text{ s}^{-1}$ , the curves show a rather large slope of the stress plateau. The shift of the stress plateau towards higher

stress values for increasing temperature follows the Clausius–Clapeyron relation. At the strain of 2%, the stress at room temperature is about 185 MPa, while it reaches about 415 MPa upon heating to 80  $^{\circ}\text{C}$ . This indicates that a maximum stress of 230 MPa can be recovered upon heating to austenite at fixed strain of 2%.

## 2.2. Design

The basic layout of the bending microactuator consists of two polymer tiles of 25  $\mu\text{m}$  thick polyimide that are interconnected by freestanding SMA hinges. Using a SMA hinge pair with double-bridge design allows for direct Joule heating by applying heating power at one tile [11]. Instead of a single SMA hinge pair used in previous work, we investigate a novel design of cascaded SMA hinge pairs as depicted in figure 3. Here, two hinge pairs with double-bridge design are connected in series and separated by a pad-like structure for intermediate electrical contacts. In the following, we will distinguish between hinge pair 1 (HP1) and 2 (HP2) and will refer to the novel design as ‘cascaded hinge design’ to discriminate between the previous ‘single hinge design’. The folding axes are approached as closely as possible, as indicated by the distance  $d$ , to keep the overall size compact compared to the single hinge design. The dimensions of the pad-like structures, connecting HP1 and HP2, are chosen as large as the remaining space provides. Furthermore, the folded overall geometry gives rise to additional in-plane flexibility, which enables accommodating stiffening effects during bending and, thus, improves bidirectional folding.

HP1 and HP2 are Joule heated for locally setting the memory shape. The temperatures for shape setting may range between 420 and 700  $^{\circ}\text{C}$  depending on heat treatment time and atmospheric conditions [35]. In this investigation, HP2 is heat treated in a constraint angle of  $+180^{\circ}$  by applying electrical interconnections as indicated by configuration 1 (green dots). For setting the memory shape of HP1, the electrical interconnections are applied as indicated by configuration 2 (red dots) and the angle of HP1 is constrained at  $+90^{\circ}$  while applying the heating current.

Important design parameters for the layout are the hinge length  $L$ , width  $w$ , and the bending radius  $R$  of the two hinge pairs. The minimal bending radius of each bridge  $R_{\min}$  depends on the thickness of the SMA film  $t_{\text{SMA}}$  of 6  $\mu\text{m}$  and the desired bending angle  $\beta$ . A rough estimate on the minimal bending radius  $R_{\min}$  can be made by assuming ideal bending conditions with a neutral axis centered in the beam cross-section [36]:

$$R_{\min} = t_{\text{SMA}}(1/|\varepsilon_{\max}| - 1)(\beta/360^{\circ})$$

As both hinge pairs contribute to active folding, it is not required for them to actuate in the full range of  $360^{\circ}$ . HP2 is heat-treated at a constraint angle of  $+180^{\circ}$  and HP1 at  $+90^{\circ}$ . The resulting angular range of the cascaded SMA hinge depends on the intrinsic stress in the SMA films giving rise to lower maximum angles compared to the constraint angles by about  $20^{\circ}$ . Therefore, the maximum achievable angles upon heating to austenite of HP2 and HP1 are about  $+160^{\circ}$



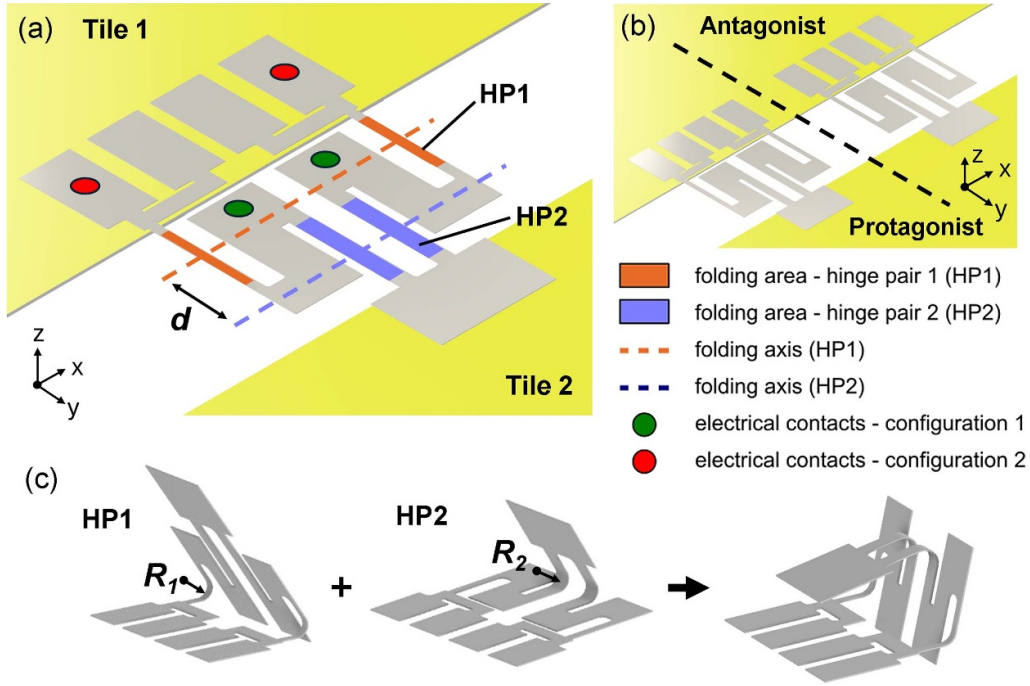


**Figure 3.** Cascaded SMA hinge design comprising two SMA hinge pairs HP1 and HP2 with double-bridge design connected in series. (a) Schematic of an individual microactuator in the initial planar state; for selective shape setting of the hinge pairs, electrical contacts are made as indicated by configuration 1 and 2;  $d$  indicates the distance between the folding axes. (b) Schematic of an antagonistic microactuator with cascaded SMA hinge design allowing for bending in opposite directions. (c) Schematic of the bending states of hinge pairs 1 and 2 and their combination. The bending radii  $R_1$  and  $R_2$  are indicated.

and  $+70^\circ$ , respectively. By taking into account the maximum recoverable strain of 3.5% [37], each hinge should be reversibly deformable by a minimum bending angle of  $\beta = 250^\circ$ . We remain below the maximum value of  $\beta = 360^\circ$ , to keep the minimum hinge length  $L_{\min} = \pi R_{\min}$  - being proportional to  $\beta$  - as short as possible. The resulting angular ranges of HP2 and HP1 then derive to  $-90^\circ \dots +160^\circ$  and  $-180^\circ \dots +70^\circ$ , respectively. Thus, in both directions the addition of the individual angles of the cascaded SMA hinge exceeds the aimed angular range of  $\pm 180^\circ$ . Based on these assumptions, the minimal bending radius is estimated to be  $R_{\min} = 115 \mu\text{m}$ . The corresponding minimal hinge length  $L_{\min}$  is determined to be  $361 \mu\text{m}$ . Consequently, we chose a hinge length  $L$  of  $400 \mu\text{m}$  for each hinge pair.

During selective shape setting of each hinge pair by Joule heating, all other hinge pairs must remain below the recrystallization temperature to avoid unintentional shape setting. For this reason, the hinge pairs are designed with different widths that are adjusted based on simulations of heat transfer as discussed below. Two additional pads on the substrate are provided for resistance monitoring during shape setting and actuation by the four-point measurement method.

### 2.3. Simulation

A coupled electro-thermal simulation model is set up in COMSOL Multiphysics for the cascaded hinge design. An electrical current is applied to the hinge pairs in the configurations 1 and 2 as shown in figure 4(a). The electric potential

field and the total generated heat are calculated by the electric current conservation equation considering the temperature-dependent electric conductivity [38]. The stationary temperature distribution is then derived by a heat transfer model taking into account heat conduction and convection. The simulation parameters are summarized in table S1 in the supplementary information. As demonstrated in figure 4(b), the hinge pairs HP1 or HP2 are selectively heated well above the critical temperature of  $400^\circ\text{C}$  for shape setting (highlighted in green) whereas the corresponding unheated hinge pair stays below the critical temperature.

IR thermography measurements are performed to validate the simulated temperature profiles upon direct Joule heating. The resolution of the IR camera is limited by a detector pitch of  $17 \mu\text{m}$ . Hence, the size of the smallest features should exceed  $50 \mu\text{m}$  in order to capture 3 pixels required to obtain a valid temperature measurement. Therefore, the experiments are performed on cascaded SMA hinges that are scaled in size by a factor of 2. The length of the hinge pairs is therefore  $800 \mu\text{m}$  while the thickness is kept at  $6 \mu\text{m}$ . The hinge pairs are covered with a black carbon spray with a coefficient of emissivity of 0.8. Figure 5(a) shows the thermal profile of the actuator measured with the IR thermography setup. Line section measurements reveal the temperature distribution at the center of the hinges. Li1 and Li6 show the temperature distribution in HP1, Li3 and Li4 show the distribution in HP2, and Li2 and Li5 show the distribution in the intermediate segment. Figure 5(b) depicts experimental and simulated temperatures along the trajectory in length direction of the cascaded hinges. The data

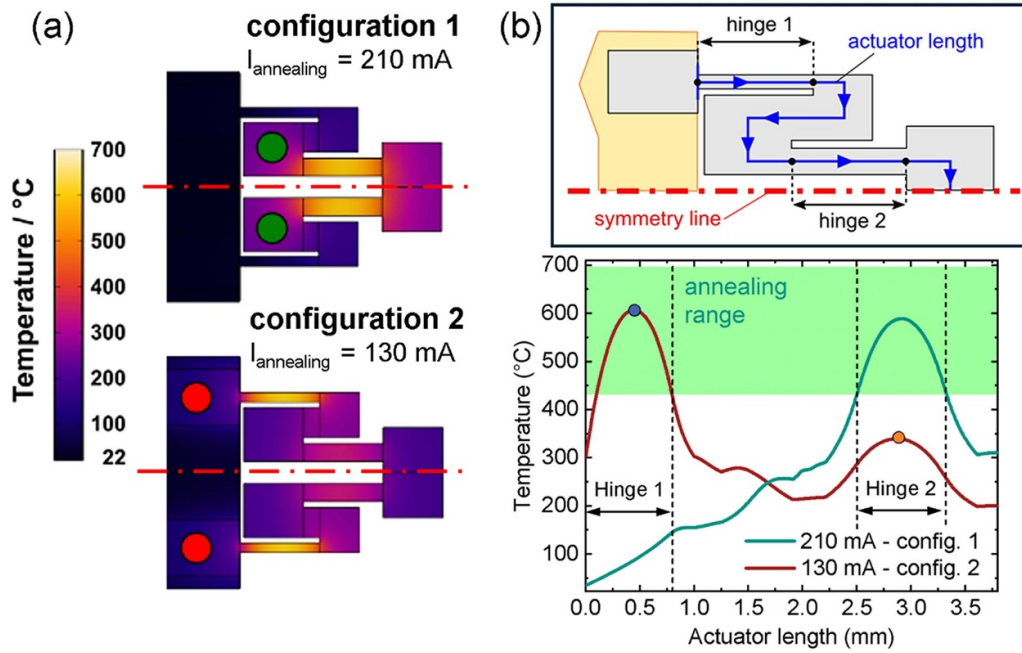


**Figure 4.** Thermal FEM simulation of the bending microactuator with cascaded hinge design. (a) Simulated temperature profiles during heat treatment in configuration 1 and 2. (b) Simulated temperature along the trajectory in length direction of the cascaded hinges as shown in the inset. Due to symmetry only half of the actuator is represented. The temperature range required for heat treatment is highlighted in green.

points of the line segments in figure 5(a) are plotted individually over the entire length of the actuator. In this case, heating currents between 13 and 40 mA are applied in configuration 2. This result shows that the FEM simulations well approximate the experimental temperature profiles caused by direct Joule heating. The experimental temperature profile reveals a minor asymmetry, which is attributed to experimental reasons as the hinge pairs are positioned in different focal planes of the IR camera. Overall, the FE model provides a good approximation of the observed temperature profiles. Therefore, it is used for model-based design of the different beam widths of HP1 and HP2 in a parametric study of the shape setting procedure.

In the following, a width of  $180 \mu\text{m}$  is chosen for HP2, while the width of HP1,  $w_{\text{HP1}}$ , is varied between 80 and  $140 \mu\text{m}$ . Figure 6 compares the maximum temperature in the hinge regions for different heating currents applied in configuration 1. Here,  $w_{\text{HP1}}$  equals  $100 \mu\text{m}$ . At a current of 130 mA, HP1 reaches a maximum temperature of around  $600^{\circ}\text{C}$ , while HP2 heats only up to  $310^{\circ}\text{C}$ . This temperature difference is large enough even if there are small deviations in the dimensions due to manufacturing tolerances. Therefore, a width ratio of  $w_1/w_2 = 0.56$  is selected for the original layout as well as for the actuator upscaled by a factor of two.

### 3. Fabrication

The bending microactuators with cascaded hinge design are fabricated by a combination of sputter deposition and photolithography, see figure 7. After sputter deposition (1) and substrate release, the freestanding TiNiCu film is heat treated (2) and subsequently laminated onto a thermal release

tape (3). Then, a Cr/Au hard mask is vapor deposited and a photoresist (PR) is spin coated (4) before the layout is exposed into the photoresist by UV direct laser writing. The Cr/Au hard mask and TiNiCu film are patterned by wet-etching (5). After removal of the photoresist and Cr/Au hard mask (6), the TiNiCu microactuators are released from the tape (7), transferred and adhesive bonded to laser-cut polyimide tiles (8).

For shape setting, the bending microactuators are fixed in a setup for selective heat treatment in constraint configuration using micro manipulators (9). For microactuators with original layout, hinge pair HP2 is heat treated in the constraint angle of  $\pm 180^{\circ}$  depending on the functionality of a protagonist or antagonist at 130 mA. Accordingly, hinge pair HP1 is heat treated in the constraint angle of  $\pm 90^{\circ}$  at 80 mA. The upscaled actuators require larger heating currents of 210 mA (HP2) and 130 mA (HP1).

### 4. Results

In the following, the bending microactuators are investigated individually and in the combination as antagonists. Individual microactuators consisting of one cascaded hinge pair allow for unidirectional folding of a tile. The combination of protagonist and antagonist consists of two cascaded hinge pairs arranged next to each other to enable bidirectional folding. All investigations on the bending microactuator are carried out in a temperature-controlled environment at  $23^{\circ}\text{C}$  and a relative humidity of approximately 50%. The actuator angles are measured using USB microscope cameras and correlated with the heating current provided by a Keysight B2900 source and measuring unit.

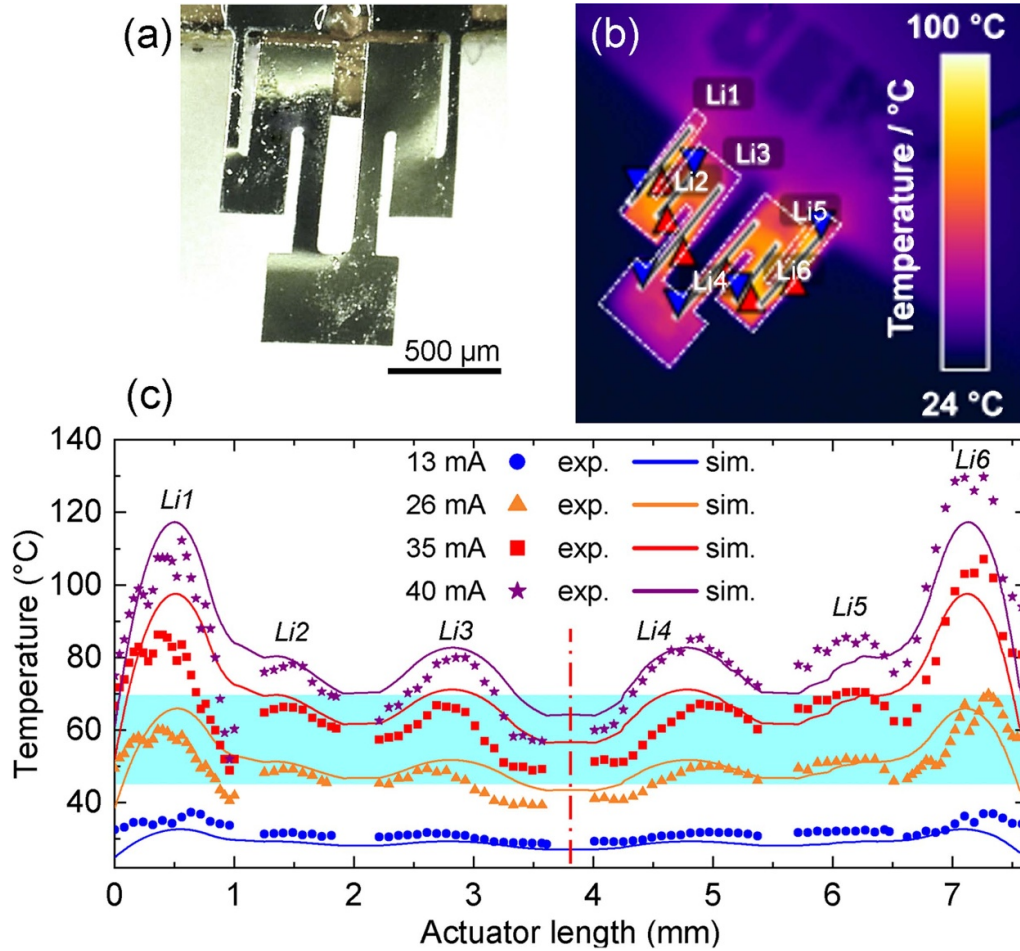


**Figure 5.** (a) Photo of a bending actuator with cascaded hinge design actuator that is scaled in size by a factor of 2 for IR measurements.;(b) IR measurement for calibration of the simulation model. Local temperature values are determined along the line sections Li1 to Li6. Blue and red arrows indicate minimal and maximal temperatures, respectively. (c) Experimental and simulated temperatures along the length direction of the cascaded hinges for different heating currents as indicated. The temperature range of martensitic phase transformation ( $M_f < T < A_f$ ) is highlighted in blue. Experimental values are determined along the line sections shown in (b). The accuracy of temperature measurement is approximately  $\pm 2$  K.

#### 4.1. Performance of individual microactuators

The hinge pairs of individual microactuators remain in their new memory shape after shape setting. In this case, the hinges are manually unfolded by means of a micro manipulator as sketched in figure S1 in the supplementary information. However, after unfolding and force release, the hinges remain quasi-plastically deformed in a remanent angle of about  $100^\circ$ . By subsequent Joule heating, this deformation can be reset and the memory shape can be recovered.

Figure 8 shows the unidirectional folding of an individual microactuator with cascaded hinge design. Starting from the remanent angle of  $100^\circ$ , the folding occurs in two steps. Hinge pair HP1 folds at heating power between 20 and 40 mW, which is rather small. The more prominent folding occurs between 70 and 80 mW at the phase transformation of hinge pair HP2. A maximal bending angle of  $181^\circ$  is observed at a heating power of about 100 mW as shown in figure 9. While stepwise reducing the heating power from its maximum value, the microactuator slightly folds back towards a remanent angle of  $162^\circ$  at 0 mW. The large difference in angular contribution of the

two hinge pairs can be attributed to three reasons: First, during the manual unfolding of the cascaded actuator by a manipulator tip, the hinge pair HP2 is more easily deformed. Thus, the quasi-plastic deformation in HP2 is larger compared to HP1. Secondly, the shape-set angle of HP2 of  $180^\circ$  is by a factor of two larger compared to HP1. Lastly, HP1 has a smaller width and, thus, provides a minor contribution per design.

#### 4.2. Performance of antagonistic microactuators

The two cascaded hinge pairs of protagonist and antagonist microactuators are heat treated individually. The protagonist is shape set to  $+180^\circ$  (HP2) and  $+90^\circ$  (HP1), whereas the antagonist is shape set to  $-180^\circ$  (HP2) and  $-90^\circ$  (HP1). In the following, the bidirectional folding performance is investigated by heating the protagonist and antagonist selectively. Figure 10 shows the folding performance of the antagonistic microactuator. The starting point of the experiment is near  $0^\circ$ . Selective heating of the antagonist initiates folding in downward direction at a heating power of about 48 mW. The



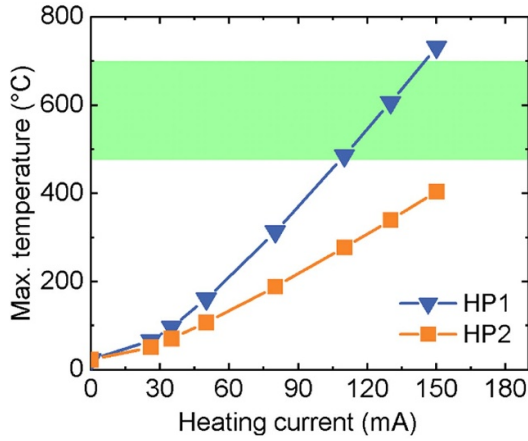


**Figure 6.** Simulated maximum temperature in hinge pairs HP1 and HP2 versus for different heating currents applied in configuration 2. The maximum temperature of hinge pair HP1 should be located in the highlighted green range, while the temperature of HP2 should stay below. The lateral dimensions of the 6  $\mu\text{m}$  thick hinge pairs are as follows:  $L = 800 \mu\text{m}$ ,  $w_{\text{HP1}} = 100 \mu\text{m}$ ,  $w_{\text{HP2}} = 180 \mu\text{m}$ ,  $w_1/w_2 = 0.56$ .

minimal folding angle of  $-105^\circ$  is reached at a heating power of 74 mW. Decreasing the heating power causes resetting to the intermediate deflection point of  $-25^\circ$ . Subsequent selective heating of the protagonist microactuator initiates folding in upward direction at a heating power of about 40 mW. The maximal folding angle of  $+107^\circ$  is reached at a heating power of 70 mW. When decreasing the heating power, the reset force of the antagonist pulls the protagonist back towards the starting point. Thus, the total bidirectional folding angle for the antagonistic microactuator is  $212^\circ$ , which is the sum of the absolute values of the minimum and maximum folding angles. After an actuation cycle, the bending microactuator does not reset to the same position. As the folding angle depends on the equilibrium of bending moments of the protagonist and the antagonist being both in martensitic state, the angular displacements exhibit a quasi-plastic non-linear behavior. Therefore, remanent strain occurs after an actuation cycle is completed resulting in the observed partial recovery of the folding angle. Figure 11 depicts photos of the antagonistic microactuator at maximal and minimal folding state when heating the antagonist (a) and protagonist (b), respectively.

For benchmarking, the performance of the bending microactuator with cascaded hinge design is compared with the previously developed bending microactuator with single hinge design. As introduced in section 2.2, the single hinge design consists of a single SMA hinge pair HP2, which is shape set for folding angles of  $\pm 180^\circ$ . Table 1 summarizes the maximal and minimal bending angles of the different microactuators. In the case of individual microactuators, the cascaded design only reveals a minor improvement in angular range due to the rather small contribution of the additional hinge pair HP1. As shown in figures S2 and S3 in the supplementary information, individual microactuators with single hinge

design start at a remanent angle of about  $+105^\circ$  similar to individual microactuators with cascaded hinge design, while the maximal folding angle is  $160^\circ$ . In the case of antagonistic microactuators, however, the cascaded design reveals a significant improvement in angular range. As shown in figures S4 and S5 in the supplementary information, selective heating of the protagonist microactuator with single hinge design causes a maximal folding angle of  $+55^\circ$ . Subsequent selective heating of the antagonist causes folding in opposite direction until a minimal angle of  $-50^\circ$  is reached. Thereby, the power range required to initiate and complete folding is about the same as for the cascaded design. In summary, the total bidirectional folding angle for the single hinge design is only  $105^\circ$  compared to  $212^\circ$  for the cascaded design.

## 5. Discussion

Bidirectional folding is essential for the development of origami-inspired systems that can change their shape or perform variable tasks autonomously. This holds particularly at miniature scales, in which the manipulation of individual tiles or manual resetting is hardly possible. Bidirectional folding will enable the development of reprogrammable matter, which can reconfigure its 3D shape without manual intervention. Here, the focus is on the development of a SMA film-based bidirectional bending microactuator enabling origami-inspired folding of tiles in small dimensions with high bending moment and small radius of curvature. Major challenges are the mechanical coupling of protagonist and antagonist SMA hinges causing unwanted impeding forces as well as thermal cross-coupling causing actuation of protagonist and antagonist at the same time, which may limit the maximum bending angle considerably. In order to enhance the angular range, we introduce a novel cascaded hinge design and investigate the corresponding mechanical and thermal properties of demonstrator systems with hinge length of 400 and 800  $\mu\text{m}$ .

For fabrication of the bending microactuator, a process flow is developed using a combination of magnetron sputtering of TiNiCu films and photolithography. The micromachined TiNiCu hinge structures are hybrid integrated on laser-cut polyimide tiles. The TiNiCu films are actuated at a strain of 2% allowing for a shape recovery stress of 230 MPa. For a bending angle  $\beta$  of  $300^\circ$  and a film thickness of 6  $\mu\text{m}$ , the minimal bending radius  $R_{\min}$  is estimated to be  $R_{\min} = 115 \mu\text{m}$ , which corresponds to a minimal hinge length of 361  $\mu\text{m}$ . The cascaded hinge design consists of two hinge pairs with double-bridge design that are connected in series and separated by a pad-like structure for intermediate electrical contacts. This design improves compliance upon bending and, thus, minimizes impeding forces due to mechanical coupling of the protagonist and antagonist.

A procedure is developed to adjust the memory shape of the hinge pairs individually and to functionalize their performance as protagonist and antagonist for bidirectional bending. The procedure includes the shape setting of each hinge pair in constraint shape by selective Joule heating at



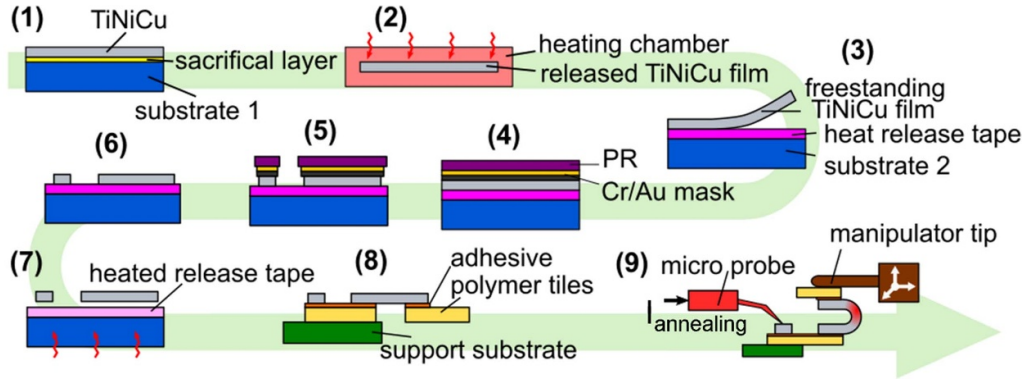


**Figure 7.** Process flow for fabrication of the bending microactuators with cascaded hinge design.

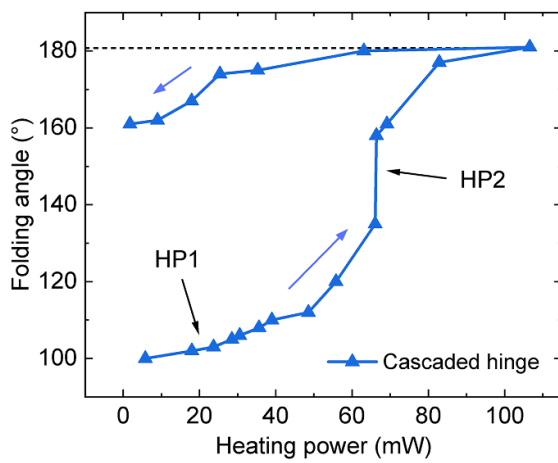


**Figure 8.** Unidirectional folding of an individual microactuator with cascaded hinge design. Folding occurs in two steps starting with hinge pair HP1 followed by hinge pair HP2 as indicated.

temperatures above 420 °C. Thereby, thermal cross-coupling must be minimized to avoid unintentional shape setting. For this reason, the hinge pairs are designed with different widths that are adjusted based on FEM simulations of the stationary temperature distribution using a heat transfer model. For a ratio of hinge widths  $w_1/w_2$  of 0.56, a sufficiently large difference of the maximum temperatures of 600 °C/310 °C can be achieved in the hinge regions to enable selective heat treatment. The simulation model is validated by comparing the simulated temperature profiles upon direct Joule heating with IR thermography measurements for a cascaded SMA hinge design that is scaled in size by a factor of 2.

For demonstration of actuator performance, the shape-set angles of the hinge pairs HP1 and HP2 are set to 90° and 180°, respectively. The unidirectional folding of individual microactuators covers an angular range between 100° and 181°, whereby hinge pair HP2 provides for the major contribution by design. The bidirectional folding of antagonistic microactuators is investigated by Joule heating the protagonist and antagonist selectively. Heating the protagonist hinge pairs causes a maximum folding angle of 107°, while the antagonist hinge

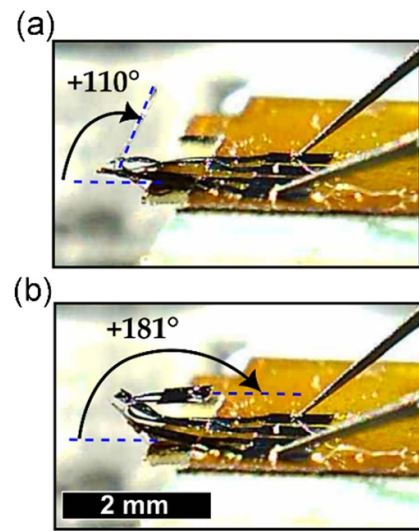


**Figure 9.** Photos of an individual microactuator with cascaded hinge design. (a) Folding angle after heating HP1 and (b) maximum folding angle after heating HP1 and HP2.

pairs exhibit a slightly smaller folding angle of −105° resulting in a total bidirectional folding angle of 212°. The bidirectional folding performance is symmetric within an accuracy of 20% reflecting the current limitations of microfabrication and shape-setting procedure for the protagonist and antagonist hinges. The achieved range of folding angles surpasses the maximum bidirectional folding angle of antagonistic SMA microactuators with single hinge design by more than a factor of two. Thereby, the power range required to initiate complete folding is about the same as for the cascaded design. Thus, the presented bending microactuator with cascaded design marks a significant improvement compared to existing miniaturized SMA folding actuators [27, 39–41].

## 6. Conclusions

We present a SMA film-based bending microactuator for Origami-Inspired bidirectional folding with large angular range using a novel antagonistic design of cascaded SMA

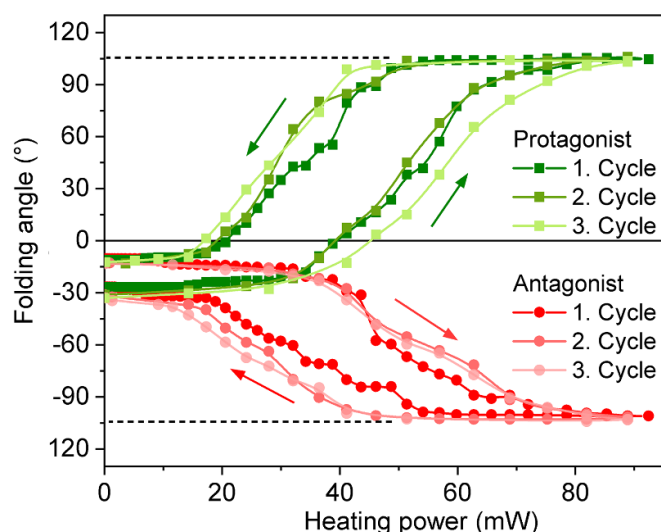


**Figure 10.** Bidirectional folding of an antagonistic microactuator with cascaded hinge design for three consecutive actuation cycles.

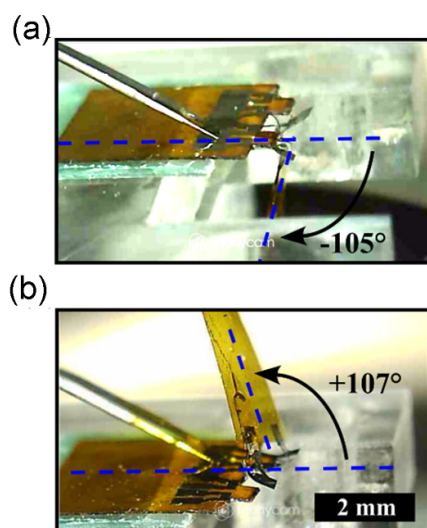


**Figure 11.** Photos of an antagonistic microactuator with cascaded hinge design. (a) Minimal folding angle when heating the antagonist, (b) maximal folding angle when heating the protagonist.

**Table 1.** Summary of maximal and minimal bending angles achieved for individual and antagonistic microactuators with cascaded design compared to corresponding microactuators with single hinge design.

	Cascaded		Single	
	Individual	Antagonistic	Individual	Antagonistic
Max	181°	+107°	160°	+55°
Min	100°	−105°	105°	−50°

hinges. Two hinge pairs with double-bridge design are connected in series and separated by a pad-like structure for intermediate electrical contacts. The microactuators are fabricated using a dedicated process flow including magnetron sputtering of TiNiCu films and photolithography. A finite element model

is introduced and validated to determine optimized hinge geometries taking the thermo-mechanical coupling of the SMA hinge pairs into account. This allows for selectively setting the memory shape of each hinge pair by selective Joule heating in constraint shape at either maximum or minimum bending angle to functionalize their performance as protagonists or antagonists. The bidirectional folding of antagonistic microactuators with cascaded hinge design reveals a total bidirectional folding angle of 212°, which is more than a factor of two compared to microactuators with single hinge design. This improvement can be attributed to the combined angular deflections of the hinge pairs and the additional flexibility of the cascaded design, as the protagonist hinge pairs can well accommodate to the folding motion of the antagonist hinge pairs. The concept of cascading opens a route for further extension of the bidirectional folding angle towards 360° by adding more double hinge pairs in series. Furthermore, the presented design consisting of two tiles may serve as a building block for more complex origami-inspired microsystems consisting of multiple tiles allowing to generate complex 3D geometries by self-folding in a reversible manner. Thereby, the major challenges will be the mastering of thermo-mechanical cross-coupling as well as the selective control of individual tiles.

### Data availability statement

The data cannot be made publicly available upon publication because they are not available in a format that is sufficiently accessible or reusable by other researchers. The data that support the findings of this study are available upon reasonable request from the authors.

### Acknowledgments

This research was funded by the German Science Foundation within the Priority Program ‘Cooperative Multistage Multistable Microactuator Systems’ (SPP2206). This work was partly carried out with the support of the Karlsruhe Nano Micro Facility (KNMF, [www.knmf.kit.edu](http://www.knmf.kit.edu)), a Helmholtz Research Infrastructure at Karlsruhe Institute of Technology (KIT, [www.kit.edu](http://www.kit.edu)). L.B. and E.Q. acknowledge funding by the German Science Foundation (DFG) through the project 413288478.

### Author contributions

Conceptualization, M.K. and L.S., methodology, data curation, formal analysis, and visualization, L.S., V.G. and L.B., simulations, L.S., writing — original draft preparation, L.S., writing — review and editing, M.K. and E.Q. All authors have read and agreed to the published version of the manuscript.

### Conflict of interest

The authors declare no competing interest.

## Appendix

### 1. Experimental

Thermal characterization is performed by differential scanning calorimetry (DSC). For SMA materials, the phase transformation from austenite to martensite is exothermic and results in a peak in the DSC curve. The area below the peak is equivalent to the latent heat of the phase transition. In this work, a Netzsch Phoenix DSC 204 is used for DSC measurements. The instrument has a temperature accuracy of  $\pm 0.1$  K. The temperature sweep rate is set to  $10 \text{ K min}^{-1}$  and a holding time of 2 min is set in between the heating and cooling cycles. The specimen mass is measured with a precision scale and ranges from 7 to 15 mg. The start and finish temperatures are evaluated by drawing tangents at the steepest parts of the two sides of the peak. The intersection of the tangents with the baseline defining the latent heat area, gives the temperature values. The heat capacity, defined as the amount of heat required to raise the temperature of the sample by 1 K, is derived according to ASTM E1269.

Further thermal characterizations, such as surface temperature profiles, are obtained by infrared thermography. The IR camera measures the heat radiated by a specimen. When the emission coefficient of the surface is known, the temperature can be derived. Here, the IR camera Teledyne FLIR A655sc is used with a macrolens and a detector pitch of  $17 \mu\text{m}$ . The absolute temperature can be measured with an accuracy of  $\pm 2$  K. Control, data acquisition, and post processing are performed with the software provided by FLIR. In experiment, the specimens under investigation are covered with a thin layer of graphite spray Kontakt Chemie Graphit 33. Its emissivity has been calibrated to 0.8.

The mechanical properties of SMAs are derived by uniaxial tensile tests. A specimen sample is clamped in between a fixed and a movable holder. The traverse of the tensile testing machine elongates the sample by moving upwards. The relative elongation  $\Delta l$  is tracked by a position sensor and the force  $F$  is measured by a load cell. For a known initial cross-section  $A_0$ , and the initial length  $L_0$ , the instantaneous engineering stress is  $\sigma = F/A_0$  and the engineering strain is  $\varepsilon = \Delta l/L_0$ . In this work, tensile tests are performed with the Zwick & Roell Z 0.5 tensile testing machine, equipped with 5 N and 50 N load cells providing a resolution of 0.002 N and 0.25 N, respectively. Deviations in the strain rate can be neglected due to the high drive resolution of  $0.055 \mu\text{m}$  and displacement control. The uncertainty of force measurement of the Xforce HP 5 N load cell is 0.4%. Deviations in the sample cross-section geometry are observed, attributable to fabrication tolerances and undercutting of  $\pm 10 \mu\text{m}$  in width  $w$ , which results in an uncertainty in the tensile stress of about  $\pm 1\%$ . In order to determine the properties of austenitic SMAs, the sample holder is placed into an in-house built heating chamber. The temperature inside the chamber is adjusted by a PID controller and additionally monitored by attaching thermocouples onto the sample holder.

The microactuators are Joule heated by ramping the electrical current of the power supply (Keysight B2900) step-wise up- and downwards under quasi-stationary conditions allowing for sufficient waiting periods between each step.

Thus, any effects of heating rate are avoided. Before the experiment, the microactuators are cycled several times to achieve a reproducible performance. The bending angles are determined using USB microscope cameras and correlated with the output of the power supply (Keysight B2900) at each step. The bending angles are then extracted from the video data using a software measurement tool (ImageJ) allowing for an accuracy of angular measurement of about  $\pm 2^\circ$ .

### 2. Finite element simulation

A coupled electro-thermal simulation model is set up in COMSOL Multiphysics (version 6.0) to optimize the cascaded actuator design. For each geometrical configuration, a current is applied on one pad and the ground is set on the other pad. The simulation parameters are summarized in table S1 in the supplementary information. The electric potential field and the total generated heat by electric heating are solved by the electric current conservation equation of the Electric Currents (ec) sub-interface. The temperature distribution along the actuator length is derived by Heat Transfer in Solids (ht) sub-interface.

### ORCID iDs

Lena Seigner  0000-0003-3724-0414  
 Vincent Gottwald  0009-0002-5946-7919  
 Lars Bumke  0000-0002-7255-0656  
 Eckhard Quandt  0000-0002-2314-5179  
 Manfred Kohl  0000-0002-0597-4440

### References

- [1] Novelino L S, Ze Q, Wu S, Paulino G H and Zhao R 2020 Untethered control of functional origami microrobots with distributed actuation *Proc. Natl Acad. Sci.* **117** 24096–101
- [2] Arun S B, Anveeth B H and Majumder A 2019 Advancements in origami inspired robots, a review 2019 2nd Int. Conf. on Intelligent Computing, Instrumentation and Control Technologies, ICICICT 2019 pp 1293–7
- [3] Nauroze S A, Novelino L S, Tentzeris M M and Paulino G H 2018 Continuous-range tunable multilayer frequency-selective surfaces using origami and inkjet printing *Proc. Natl Acad. Sci. USA* **115** 13210–5
- [4] Yang Y et al 2024 A review of multimaterial additively manufactured electronics and 4-D printing/origami shape-memory devices: design, fabrication, and implementation *Proc. IEEE* **112** 954–99
- [5] Lv C, Krishnaraju D, Konjevod G, Yu H and Jiang H 2014 Origami based mechanical metamaterials *Sci. Rep.* **4** 5979
- [6] Velvaluri P, Soor A, Plucinsky P, de Miranda R L, James R D and Quandt E 2021 Origami-inspired thin-film shape memory alloy devices *Sci. Rep.* **11** 10988
- [7] Wu J, Guo X, Pan X, Hua J, Cen Y, Li S, Huang F, Zhang F, Pan L and Shi Y 2025 Origami-kirigami structures and its applications in biomedical devices *Biomed. Mater. Devices* **3** 45–61
- [8] Hernandez E A P, Hartl D J and Lagoudas D C 2019 *Active Origami: Modeling, Design, and Applications* (Springer)
- [9] Felton S M, Becker K P, Aukes D M and Wood R J 2015 Self-folding with shape memory composites at the millimeter scale *J. Micromech. Microeng.* **25** 085004

- [10] Rojas S, Riley K S and Arrieta A F 2022 Multistable bioinspired origami with reprogrammable self-folding *J. R. Soc. Interface* **19** 20220426
- [11] Peraza-Hernandez E A, Hartl D J, Malak Jr J R J and Lagoudas D C 2014 Origami-inspired active structures: a synthesis and review *Smart Mater. Struct.* **23** 094001
- [12] Kohl M 2013 *Shape Memory Microactuators* (Springer)
- [13] Chen J, Ding Q, Kim Y and Cheng S S 2022 Design, modeling and evaluation of a millimeter-scale SMA bending actuator with variable length *J. Intell. Mater. Syst. Struct.* **33** 942–57
- [14] Lee Y J, Abdelrahman M K, Kalairaj M S and Ware T H 2023 Self-assembled microactuators using chiral liquid crystal elastomers *Small* **19** 2302774
- [15] Wang Y, Ye H, He J, Ge Q and Xiong Y 2024 Electrothermally controlled origami fabricated by 4D printing of continuous fiber-reinforced composites *Nat. Commun.* **15** 2322
- [16] Bechtold C, de Miranda R L, Chluba C and Quandt E 2016 Fabrication of self-expandable NiTi thin film devices with micro-electrode array for bioelectric sensing, stimulation and ablation *Biomed. Microdevices* **18** 106
- [17] Lima de Miranda R, Zamponi C and Quandt E 2009 Fabrication of TiNi thin film stents *Smart Mater. Struct.* **18** 104010
- [18] Curtis S M, Gugat J L, Bumke L, Dengiz D, Seigner L, Schmadel D, Lazarus N S and Quandt E 2023 Thin-film superelastic alloys for stretchable electronics *Shap. Mem. Superelasticity* **9** 35–49
- [19] Dengiz D, Goldbeck H, Curtis S M, Bumke L, Jetter J and Quandt E 2023 Shape memory alloy thin film auxetic structures *Adv. Mater. Technol.* **8** 2201991
- [20] Kohl M, Dittmann D, Quandt E and Winzek B 2000 Thin film shape memory microvalves with adjustable operation temperature *Sens. Actuators A* **83** 214–9
- [21] Megnin C, Barth J and Kohl M 2012 A bistable SMA microvalve for 3/2-way control *Sens. Actuators A* **188** 285–91
- [22] An B and Rus D 2014 Designing and programming self-folding sheets *Robot. Auton. Syst.* **62** 976–1001
- [23] Hawkes E, An B, Benbernou N M, Tanaka H, Kim S, Demaine E D, Rus D and Wood R J 2010 Programmable matter by folding *Proc. Natl Acad. Sci. USA* **107** 12441–5
- [24] Chafik A A, Gaber J, Tayane S, Ennaji M, Bourgeois J and Ghazawi T E 2024 From conventional to programmable matter systems: a review of design, materials, and technologies *ACM Comput. Surv.* **56** 210:1–210:26
- [25] Cheng Y, Wang J, Li R, Gu X, Zhang Y, Zhu J and Zhang W 2024 Design and prototype testing of a smart SMA actuator for UAV foldable tail wings *Actuators* **13** 499
- [26] Park J J, Won P and Ko S H 2019 A review on hierarchical origami and kirigami structure for engineering applications *Int. J. Precis. Eng. Manuf.—Green Technol.* **6** 47–161
- [27] Hu K, Rabenoroso K and Ouisse M 2021 A review of SMA-based actuators for bidirectional rotational motion: application to origami robots *Front. Robot. AI* **8** 678486
- [28] Firouzeh A and Paik J 2015 Robogami: a fully integrated low-profile robotic origami *J. Mech. Robot.* **7** 021009
- [29] Park Y J, Ahn H and Rodrigue H 2024 Shape-memory alloy-based auxetic smart metamaterials: enabling inherently bidirectional actuation *Adv. Intell. Syst.* **6** 2400040
- [30] Seigner L, Bezsmertna O, Fähler S, Tshikwand G K, Wendler F and Kohl M 2020 Origami-inspired shape memory folding microactuator *Proceedings* **64** 6
- [31] Seigner L, Tshikwand G K, Wendler F and Kohl M 2021 Bi-directional origami-inspired SMA folding microactuator *Actuators* **10** 181
- [32] Kohl M et al 2025 Active bi- and multistability in cooperative microactuator systems *Sens. Actuators Rep.* **9** 100338
- [33] Gu H, Bumke L, Chluba C, Quandt E and James R D 2018 Phase engineering and supercompatibility of shape memory alloys *Mater. Today* **21** 265–77
- [34] Lima de Miranda R, Zamponi C and Quandt E 2013 Micropatterned freestanding superelastic TiNi Films *Adv. Eng. Mater.* **15** 66–69
- [35] Fu Y, Du H, Zhang S and Gu Y 2005 Stress and surface morphology of TiNiCu thin films: effect of annealing temperature *Surf. Coat. Technol.* **198** 389–94
- [36] Timoshenko S P, Goodier J N and Abramson H N 1970 Theory of elasticity 3rd edn *J. Appl. Mech.* **37** 888
- [37] Chen X, Bumke L, Quandt E and Kohl M 2023 Bistable actuation based on antagonistic buckling SMA beams *Actuators* **12** 422
- [38] Arivanandhan G, Li Z, Curtis S M, Hanke L, Quandt E and Kohl M 2023 Power optimization of TiNiHf/Si shape memory microactuators *Actuators* **12** 82
- [39] Kim Y, Jang T, Gurung H, Mansour N A, Ryu B and Shin B 2019 Bidirectional rotating actuators using shape memory alloy wires *Sens. Actuators A* **295** 512–22
- [40] Wang W, Rodrigue H and Ahn S-H 2016 Deployable soft composite structures *Sci. Rep.* **6** 20869
- [41] Paik J K and Wood R J 2012 A bidirectional shape memory alloy folding actuator *Smart Mater. Struct.* **21** 065013